Electromagnetic Field Behavior of 3D Maxwell's Equations for Chiral Media

Tsung-Ming Huang[a], Tiexiang Li[b,*], Ruey-Lin Chern[c], Wen-Wei Lin[d]

[a]*Department of Mathematics, National Taiwan Normal University, Taipei 116, Taiwan.*
E-mail: `min@ntnu.edu.tw`*.*
[b]*School of Mathematics, Southeast University, Nanjing 211189, People's Republic of China.*
E-mail: `txli@seu.edu.cn`*.*
[c]*Institute of Applied Mechanics, National Taiwan University, Taipei 106, Taiwan. E-mail:*
`chernrl@ntu.edu.tw`*.*
[d]*Department of Applied Mathematics, National Chiao Tung University, Hsinchu 300,*
Taiwan. E-mail: `wwlin@math.nctu.edu.tw`*.*

Abstract

This article focuses on numerically studying the eigenstructure behavior of generalized eigenvalue problems (GEPs) arising in three dimensional (3D) source-free Maxwell's equations with magnetoelectric coupling effects which model 3D reciprocal chiral media. It is challenging to solve such a large-scale GEP efficiently. We combine the null-space free method with the inexact shift-invert residual Arnoldi method and MINRES linear solver to solve the GEP with a matrix dimension as large as 5,308,416. The eigenstructure is heavily determined by the chirality parameter γ. We show that all the eigenvalues are real and finite for a small chirality γ. For a critical value $\gamma = \gamma^*$, the GEP has 2×2 Jordan blocks at infinity eigenvalues. Numerical results demonstrate that when γ increases from γ^*, the 2×2 Jordan block will first split into a complex conjugate eigenpair, then rapidly collide with the real axis and bifurcate into positive (resonance) and negative eigenvalues with modulus smaller than the other existing positive eigenvalues. The resonance band also exhibits an anticrossing interaction. Moreover, the electric and magnetic fields of the resonance modes are localized inside the structure, with only a slight amount of field leaking into the background (dielectric) material.

Keywords: Maxwell's equations, three-dimensional chiral medium, null-space free eigenvalue problem, shift-invert residual Arnoldi method, anticrossing eigencurves, resonance mode

*Corresponding author
Email address:* `txli@seu.edu.cn` (Tiexiang Li)

1. Introduction

Mathematically, the propagation of electromagnetic fields in bianisotropic media is modelled by the three-dimensional (3D) frequency domain source-free Maxwell's equations with the constitutive relations

$$\nabla \times \boldsymbol{E}(\mathbf{x}) = \iota\omega\boldsymbol{B}(\mathbf{x}), \qquad\qquad \nabla \cdot \boldsymbol{B}(\mathbf{x}) = 0, \qquad (1.1a)$$

$$\nabla \times \boldsymbol{H}(\mathbf{x}) = -\iota\omega\boldsymbol{D}(\mathbf{x}), \qquad\qquad \nabla \cdot \boldsymbol{D}(\mathbf{x}) = 0, \qquad (1.1b)$$

where ω is the frequency, $\boldsymbol{E}$, $\boldsymbol{H}$, $\boldsymbol{D}$ and $\boldsymbol{B}$ are the electric, the magnetic fields, the dielectric displacement and the magnetic induction, respectively, at the position $\mathbf{x} \in \mathbb{R}^3$. Bianisotropic materials are important classes of complex media of which the coupling effects between electric and magnetic fields can be described by the constitutive relations

$$\boldsymbol{B} = \tilde{\mu}\boldsymbol{H} + \tilde{\zeta}\boldsymbol{E}, \quad \boldsymbol{D} = \tilde{\varepsilon}\boldsymbol{E} + \tilde{\xi}\boldsymbol{H}, \qquad (1.2)$$

where $\tilde{\mu}$ is the permeability, $\tilde{\varepsilon}$ is the permittivity, $\tilde{\zeta}$ and $\tilde{\xi}$ are magnetoelectric parameters. For detailed descriptions of bianisotropic materials with respect to (1.2), we refer to [1, 2, 3, 4, 5, 6, 22, 24, 25] and references therein.

If the photonic crystal is made of complex media that contain magneto-electric couplings in (1.2), that is, the electric (magnetic) polarization being induced by the magnetic (electric) field, the eigensystem distinctly differs from the classical one: the single curl, as well as the double curl operator, appears in the wave equations [7, 21]. This feature corresponds to the symmetry breaking in the system and introduces chirality in the eigensystem. It is expected that circularly or elliptically polarized waves will serve as eigenwaves in the system. To solve the band structures for this type of photonic crystals, in particular, in three dimensions, extra care has to be taken on the choice of the range space with the single curl operator.

The magnetoelectric coupling coefficients $\tilde{\mu}, \tilde{\varepsilon}, \tilde{\zeta}$ and $\tilde{\xi}$ in (1.2) are usually tensor matrices in various forms [19, 23]. In particular, a bianisotropic medium is also called a biisotropic medium, if $\tilde{\mu}, \tilde{\varepsilon}, \tilde{\zeta}$ and $\tilde{\xi}$ are scalar dyadics, or equivalently,

$$\tilde{\mu} = \mu_0\tilde{I}, \ \tilde{\varepsilon} = \varepsilon(\mathbf{x})\tilde{I}, \ \tilde{\zeta} = \zeta(\mathbf{x})\tilde{I}, \ \tilde{\xi} = \xi(\mathbf{x})\tilde{I}, \qquad (1.3)$$

where $\tilde{I}$ is the identity dyadics, $\mu_0 \equiv 1$, specially, the permittivity $\varepsilon(\mathbf{x})$ and the reciprocal chiral medium (Pasteur medium) $\zeta(\mathbf{x}), \xi(\mathbf{x})$ in (1.3) which we are interested in this paper, are types of biisotropic media with

$$\varepsilon(\mathbf{x}) = \begin{cases} \varepsilon_i, \ \mathbf{x} \in \text{material}, \\ \varepsilon_0, \ \text{otherwise}, \end{cases} \qquad\qquad (1.4a)$$

$$\zeta(\mathbf{x}) = \begin{cases} -\iota\gamma, \ \mathbf{x} \in \text{material}, \\ 0, \ \text{otherwise}, \end{cases} \qquad \xi(\mathbf{x}) = \begin{cases} \iota\gamma, \ \mathbf{x} \in \text{material}, \\ 0, \ \text{otherwise}, \end{cases} \qquad (1.4b)$$

and $\varepsilon_0 > 0$, $\varepsilon_i > 0$, $\gamma \geq 0$.

The Maxwell's equations (1.1) together with (1.2) can be rewritten as

$$
\begin{bmatrix} 0 & -\iota\nabla\times \\ \iota\nabla\times & 0 \end{bmatrix} \begin{bmatrix} \boldsymbol{H} \\ \boldsymbol{E} \end{bmatrix} = \omega \begin{bmatrix} \tilde{\mu} & \tilde{\zeta} \\ \tilde{\xi} & \tilde{\varepsilon} \end{bmatrix} \begin{bmatrix} \boldsymbol{H} \\ \boldsymbol{E} \end{bmatrix}. \tag{1.5}
$$

Based on the Bloch Theorem [18, p.167], the eigenvectors $\boldsymbol{E}$ and $\boldsymbol{H}$ on a given crystal lattice, satisfying the quasi-periodic conditions

$$
\boldsymbol{E}(\mathbf{x} + \mathbf{a}_l) = e^{\iota 2\pi \mathbf{k}\cdot\mathbf{a}_l} \boldsymbol{E}(\mathbf{x}), \ \boldsymbol{H}(\mathbf{x} + \mathbf{a}_l) = e^{\iota 2\pi \mathbf{k}\cdot\mathbf{a}_l} \boldsymbol{H}(\mathbf{x}), \tag{1.6}
$$

are of interest, where $2\pi\mathbf{k}$ is the Bloch wave vector in the first Brillouin zone $\mathcal{B}$ and $\mathbf{a}_l$, $l = 1, 2, 3$ are the lattice translation vectors (e.g. [17, p.34]). Using Yee's finite difference scheme [26] on (1.5) satisfying the source-free conditions and the quasi-periodic conditions (1.6), the discretized Maxwell's equations with biisotropic media (1.4) result in a generalized eigenvalue problem (GEP) in the form

$$
\begin{bmatrix} 0 & -\iota C \\ \iota C^H & 0 \end{bmatrix} \begin{bmatrix} \mathbf{h} \\ \mathbf{e} \end{bmatrix} = \omega \begin{bmatrix} \mu_d & \zeta_d \\ \xi_d & \varepsilon_d \end{bmatrix} \begin{bmatrix} \mathbf{h} \\ \mathbf{e} \end{bmatrix}, \tag{1.7}
$$

where $\mathbf{h}, \mathbf{e} \in \mathbb{C}^{3n}$, $\mu_d, \varepsilon_d, \xi_d, \zeta_d$, and $C \in \mathbb{C}^{3n \times 3n}$ with C having the special structure which can easily be treated with the fast Fourier transform (FFT) to accelerate the numerical simulation [8, 11] (see Section 2 for details).

In the presence of the chirality parameter γ in (1.4b), the degeneracy between the first two bands has been lifted, that is, the two bands are no longer degenerate [8, Figures 2 and 5], as a result of the symmetry breaking in the constitutive relation. As γ increases, a larger discrepancy is found between the two bands. For any two Hermitian matrices A and B, we say that the matrix pair (A, B) or the matrix pencil $A - \omega B$ is positive definite if B is positive definite. All eigenvalues of positive definite matrix pair (A, B) are real. For photonic crystals made of isotropic chiral media (1.4) with a small chirality γ, namely, the weakly-coupled case, the matrix pair in (1.7) is positive definite for which efficient numerical algorithms and band structures have been well-studied by Chern et al [8]. A critical condition occurs when the chirality parameter is equal to the square root of the permittivity ε_i in (1.4a), where the constitutive matrix is no longer positive definite [8]. In this situation, the right-hand side coefficient matrix $\begin{bmatrix} \mu_d & \zeta_d \\ \xi_d & \varepsilon_d \end{bmatrix}$ in (1.7) becomes singular. When the chirality parameter exceeds the critical value, the matrix pairs in (1.7) may introduce very different and complicated eigenstructures. As shown in Section 5, such eigenstructures lead to the following two new interesting physical phenomena.

- The band structure changes so drastically that a large number of resonance modes emerge from lower frequencies due to the bifurcation of eigenvalues, pushing the original modes to higher frequencies. The resonance modes tend to be dispersionless, that is, insensitive to the change of wave vectors, and are represented by flat bands. In particular, each of the resonance bands exhibits an anticrossing (avoided crossing) interaction with the original one.

- A distinguished feature of the resonance mode is that the electromagnetic fields are highly concentrated inside the chiral material, with only a slight amount of fields leaking into the background (dielectric) material. In a homogeneous chiral medium characterized by the dielectric constant ε and chirality parameter γ, there are two *effective* refractive indices $\sqrt{\varepsilon} + \gamma$ and $\sqrt{\varepsilon} - \gamma$ [7]. For a larger γ such that $\gamma > \sqrt{\varepsilon}$, $\sqrt{\varepsilon} + \gamma$ becomes even larger and the chiral medium behaves as a waveguide when it is surrounded by the medium with a lower refractive index. In this situation, most fields will be concentrated in the region with a higher refractive index, leading to the so-called *waveguide mode*. On the other hand, $\sqrt{\varepsilon} - \gamma$ becomes negative and the chiral medium behaves like a negative index material. When it is connected to the background with a positive refractive index, the fields will be concentrated at the interface, leading to the so-called *surface mode*. In the present problem, the emerging resonance modes are basically a combination of waveguide modes and surface modes, with the fields highly localized in the structure and slightly smeared to the background. This is considered a unique feature of the eigenmodes in the chiral photonic crystals when the chirality parameter goes beyond the critical value.

However, how to solve the GEP (1.7) with the chirality parameter greater than the critical value, namely, the strongly-coupled case, efficiently is still open. The difficulty is that the matrix pair in (1.7) is no longer a positive definite matrix pair which may introduce a very different and complicated eigenstructure. Numerical results by newly developed algorithms (see Section 4) show that the matrix pair of (1.7) can create some new state whose energy (frequency) is smaller to that of the original ground state.

In this paper, we make the following contribution on the 3D Maxwell's equations with strongly coupled reciprocal chiral media:

- For a critical value $\gamma = \gamma^*$, the matrix pair in (1.7) becomes positive semidefinite such that null spaces of both matrices in (1.7) generically have no non-trivial intersection (this property always holds in our practical applications), and has 2×2 Jordan blocks at $\omega = \infty$.

- For $\gamma = \gamma^* + 0^+$, the matrix pair in (1.7) creates lots of complex conjugate eigenvalue pairs near $\pm \iota \infty$ which rapidly collide with the real axis at $\gamma \equiv \gamma^1 > \gamma^*$ and bifurcate into positive (resonance) and negative eigenvalues with modulus smaller than the other existing positive eigenvalues. The newly created positive eigenmode pushes the original modes to higher frequencies.

- We use the shift-invert residual Arnoldi (SIRA) method [16, 20] combined with MINRES [10] and the FFT-based scheme [11] to find a few smallest positive eigenvalues of (1.7) for $\gamma > \gamma^*$ and show that the associated fields are highly localized in the structure and slightly smeared to the background material. Numerical experiments also show that the resonance band and the original band exhibit an anticrossing interaction.

4

This paper is outlined as follows. In Section 2, we briefly introduce the matrix representation of the discretization of Maxwell's equations and the associated singular value decomposition. In Section 3, we analyze and discuss the eigenstructure behavior of discretized Maxwell's equations. A null-space free method and shift-invert residual Arnoldi method are introduced in Section 4 to solve the GEP (1.7). Numerical results are demonstrated in Section 5 to show the iteration numbers of the eigensolver, colliding eigenvalues, anticrossing eigencurves and condensations of eigenvectors. Finally, a concluding remark is given in Section 6.

Notation. Bold letters denote vectors; $\iota = \sqrt{-1}$ is the imaginary unit; I_n is the identity matrix of size n; $I^{(i)} \in \mathbb{R}^{3n \times 3n}$ denotes the diagonal matrix with the j-th diagonal entry being 1 for the corresponding j-th discrete point inside the material and zero otherwise; $I^{(0)} = I_{3n} - I^{(i)}$; $\widehat{I}^{(0)}$ and $\widehat{I}^{(i)}$ denote the matrices consisting of all nonzero columns of $I^{(0)}$ and $I^{(i)}$, respectively. For matrices A and B, $A^\top$ and A^H are the transpose and conjugate transpose, respectively; $\mathcal{N}(A)$ and $\mathcal{R}(A)$ are the null space and the range space of A, respectively; $A \otimes B$ and $A \oplus B = \mathrm{diag}(A, B)$ are, respectively, the Kronecker product and the direct sum of A and B (with suitable sizes).

2. Discretization of Maxwell's equations

From crystallography, it is well-known that crystal structures can be classified as 14 Bravais lattices. Because of various lattices, the matrix C in (1.7) of the discretized single-curl operator on the electric field may have different forms. To look through the details of the discretization process of Yee's scheme for Maxwell's equations (1.5) with three-dimensional photonic crystals, we refer the reader to [14]. For convenience, in this paper, we only consider the face centered cubic (FCC) lattice with

$$\mathbf{a}_1 = \frac{a}{\sqrt{2}}[1, 0, 0]^\top, \mathbf{a}_2 = \frac{a}{\sqrt{2}}\left[\frac{1}{2}, \frac{\sqrt{3}}{2}, 0\right]^\top, \mathbf{a}_3 = \frac{a}{\sqrt{2}}\left[\frac{1}{2}, \frac{2}{2\sqrt{3}}, \sqrt{\frac{2}{3}}\right]^\top, \quad (2.1)$$

where a is the lattice constant. Let n_1, n_2 and n_3 denote the numbers of grid points in the x_1-, x_2- and x_3- axis, respectively. Set $\delta_1 = \frac{a}{n_1\sqrt{2}}$, $\delta_2 = \frac{a\sqrt{3}}{n_2 2\sqrt{2}}$, $\delta_3 = \frac{a}{n_3\sqrt{3}}$, the associated mesh lengths, and $n = n_1 n_2 n_3$. Then the resulting $3n \times 3n$ matrix C is of the form [11, 12]

$$C = \begin{bmatrix} 0 & -C_3 & C_2 \\ C_3 & 0 & -C_1 \\ -C_2 & C_1 & 0 \end{bmatrix}, \quad (2.2)$$

where

$$C_1 = \frac{1}{\delta_1} I_{n_2 n_3} \otimes K_{1,n_1}(e^{\iota 2\pi \mathbf{k} \cdot \mathbf{a}_1}), \quad (2.3\text{a})$$

$$C_2 = \frac{1}{\delta_2} I_{n_3} \otimes K_{n_1,n_2}(e^{\iota 2\pi \mathbf{k} \cdot \mathbf{a}_2} J_1), \quad (2.3\text{b})$$

$$C_3 = \frac{1}{\delta_3} K_{n_1 n_2, n_3}(e^{\iota 2\pi \mathbf{k} \cdot \mathbf{a}_3} J_2) \quad (2.3\text{c})$$

with $2\pi\mathbf{k}$ being Bloch wave vectors as in (1.6),

$$J_1 = \begin{bmatrix} 0 & e^{-\iota 2\pi\mathbf{k}\cdot\mathbf{a}_1}I_{n_1/2} \\ I_{n_1/2} & 0 \end{bmatrix}, \tag{2.4a}$$

$$J_2 = \begin{bmatrix} 0 & e^{-\iota 2\pi\mathbf{k}\cdot\mathbf{a}_2}I_{n_2/3}\otimes I_{n_1} \\ I_{2n_2/3}\otimes J_1 & 0 \end{bmatrix}, \tag{2.4b}$$

and

$$K_{m_1,m_2}(X) = \begin{bmatrix} -I_{m_1} & I_{m_1} & & \\ & \ddots & \ddots & \\ & & -I_{m_1} & I_{m_1} \\ X & & & -I_{m_1} \end{bmatrix} \in \mathbb{C}^{m_1 m_2 \times m_1 m_2}. \tag{2.4c}$$

It has been shown in [11] that the matrices C_1, C_2, and C_3 can be diagonalized by a common unitary matrix as in Theorem 2.1.

Theorem 2.1 (Eigendecompositions of C_i's [11]). *The matrices C_1, C_2 and C_3 in (2.3) are simultaneously diagonalizable by the unitary matrix $T = \frac{1}{\sqrt{n_1 n_2 n_3}}[T_1, T_2,$ $\cdots, T_{n_1}]$ with $T_i = [T_{i,1}, \cdots, T_{i,n_2}]$ and $T_{i,j} = [\mathbf{z}_{i,j,1}\otimes\mathbf{y}_{i,j}\otimes\mathbf{x}_i, \cdots, \mathbf{z}_{i,j,n_3}\otimes \mathbf{y}_{i,j}\otimes\mathbf{x}_i]$, in the forms*

$$T^H C_1 T = \Lambda_{n_1}\otimes I_{n_2 n_3} \equiv \Lambda_1, \tag{2.5a}$$

$$T^H C_2 T = \oplus_{i=1}^{n_1}(\Lambda_{i,n_2}\otimes I_{n_3}) \equiv \Lambda_2, \tag{2.5b}$$

$$T^H C_3 T = (\oplus_{i=1}^{n_1}\oplus_{j=1}^{n_2}\Lambda_{i,j,n_3}) \equiv \Lambda_3, \tag{2.5c}$$

where

$$\Lambda_{n_1} = \delta_1{}^{-1}\mathrm{diag}\left(e^{\theta_1}-1,\cdots,e^{\theta_{n_1}}-1\right), \tag{2.5d}$$

$$\Lambda_{i,n_2} = \delta_2{}^{-1}\mathrm{diag}\left(e^{\theta_{i,1}}-1,\cdots,e^{\theta_{i,n_2}}-1\right), \tag{2.5e}$$

$$\Lambda_{i,j,n_3} = \delta_3{}^{-1}\mathrm{diag}\left(e^{\theta_{i,j,1}}-1,\cdots,e^{\theta_{i,j,n_3}}-1\right), \tag{2.5f}$$

and

$$\begin{cases} \theta_i = \frac{\iota 2\pi(i+\mathbf{k}\cdot\mathbf{a}_1)}{n_1}, \\ \mathbf{x}_i = \left[1, e^{\theta_i},\cdots, e^{(n_1-1)\theta_i}\right]^\top, \end{cases} \tag{2.5g}$$

$$\begin{cases} \theta_{i,j} = \frac{\iota 2\pi(j-\frac{i}{2}+\mathbf{k}\cdot\widehat{\mathbf{a}}_2)}{n_2} \;\; with \; \widehat{\mathbf{a}}_2 = \mathbf{a}_2 - \frac{1}{2}\mathbf{a}_1, \\ \mathbf{y}_{i,j} = \left[1, e^{\theta_{i,j}},\cdots, e^{(n_2-1)\theta_{i,j}}\right]^\top, \end{cases} \tag{2.5h}$$

$$\begin{cases} \theta_{i,j,k} = \frac{\iota 2\pi(k-\frac{1}{3}(i+j)+\mathbf{k}\cdot\widehat{\mathbf{a}}_3)}{n_3} \;\; with \; \widehat{\mathbf{a}}_3 = \mathbf{a}_3 - \frac{1}{3}(\mathbf{a}_1+\mathbf{a}_2), \\ \mathbf{z}_{i,j,k} = \left[1, e^{\theta_{i,j,k}},\cdots, e^{(n_3-1)\theta_{i,j,k}}\right]^\top, \end{cases} \tag{2.5i}$$

for $i = 1,\cdots, n_1$, $j = 1,\cdots, n_2$, $k = 1,\cdots, n_3$.

The following important singular value decomposition of C is derived in [8].

Theorem 2.2 ([8]). *There exist unitary matrices*

$$Q = \begin{bmatrix} Q_r & Q_0 \end{bmatrix} \equiv (I_3 \otimes T) \begin{bmatrix} \Pi_1 & \Pi_2 \mid \Pi_0 \end{bmatrix} \equiv (I_3 \otimes T) \begin{bmatrix} \Pi_{1,1} & \Pi_{1,2} & \Pi_{1,0} \\ \Pi_{2,1} & \Pi_{2,2} & \Pi_{2,0} \\ \Pi_{3,1} & \Pi_{3,2} & \Pi_{3,0} \end{bmatrix},$$

$$\text{(2.6a)}$$

$$P = \begin{bmatrix} P_r & P_0 \end{bmatrix} = (I_3 \otimes T) \begin{bmatrix} -\bar{\Pi}_2 & \bar{\Pi}_1 \mid \bar{\Pi}_0 \end{bmatrix}, \tag{2.6b}$$

where $Q_r, P_r \in \mathbb{C}^{3n \times 2n}$ and $\Pi_{i,j} \in \mathbb{C}^{n \times n}$, $i = 1, 2, 3, j = 0, 1, 2$, are diagonal such that C has a singular value decomposition

$$C = P \, diag(\Lambda_q^{1/2}, \Lambda_q^{1/2}, 0) Q^H = P_r \Sigma_r Q_r^H, \quad \Sigma_r = diag(\Lambda_q^{1/2}, \Lambda_q^{1/2}) \tag{2.7}$$

with $\Lambda_q = \Lambda_1^H \Lambda_1 + \Lambda_2^H \Lambda_2 + \Lambda_3^H \Lambda_3$.

We now consider the discretization of the right hand side in (1.7). The diagonal matrices μ_d, ε_d, ξ_d and ζ_d in (1.7) can be determined by the shape of the medium. From (1.3) and (1.4) we have

$$\mu_d = I_{3n}, \qquad\qquad \varepsilon_d = \varepsilon_0 I^{(0)} + \varepsilon_i I^{(i)}, \tag{2.8a}$$

$$\zeta_d = -\iota \gamma I^{(i)}, \qquad\qquad \xi_d = \iota \gamma I^{(i)}, \tag{2.8b}$$

where ε_i, ε_0 are the permittivites inside and outside the medium, respectively, $\gamma > 0$ is the chirality, $I^{(0)}$ and $I^{(i)}$ are defined in Notations of Section 1.

3. Eigenstructure behaviour of discretized Maxwell's equations

We now study the eigenstructure behaviour of the GEP in (1.7). It is easily seen that equation (1.7) can be rewritten as

$$\begin{bmatrix} I_{3n} & 0 \\ \xi_d \mu_d^{-1} & I_{3n} \end{bmatrix} \left(\begin{bmatrix} 0 & -\iota C \\ \iota C^H & \iota \xi_d \mu_d^{-1} C - \iota C^H \mu_d^{-1} \zeta_d \end{bmatrix} \right.$$
$$\left. - \omega \begin{bmatrix} \mu_d & 0 \\ 0 & \varepsilon_d - \xi_d \mu_d^{-1} \zeta_d \end{bmatrix} \right) \begin{bmatrix} I_{3n} & \mu_d^{-1} \zeta_d \\ 0 & I_{3n} \end{bmatrix} \begin{bmatrix} \mathbf{h} \\ \mathbf{e} \end{bmatrix} = 0. \tag{3.1}$$

Together with the choices of $\mu_d, \varepsilon_d, \xi_d, \zeta_d$ as in (2.8), we have the following matrix pencil instead.

$$\begin{bmatrix} 0 & -\iota C \\ \iota C^H & -\gamma [I^{(i)} C + C^H I^{(i)}] \end{bmatrix}$$
$$- \omega \begin{bmatrix} I_{3n} & 0 \\ 0 & \varepsilon_0 I^{(0)} + (\varepsilon_i - \gamma^2) I^{(i)} \end{bmatrix} \equiv A_\gamma - \omega B_\gamma. \tag{3.2}$$

Furthermore, it is easily seen that $(\omega, \begin{bmatrix} \mathbf{h} \\ \mathbf{e} \end{bmatrix})$ is an eigenpair of (1.7) if and only if $(\omega, \begin{bmatrix} \mathbf{h} - \iota \gamma I^{(i)} \mathbf{e} \\ \mathbf{e} \end{bmatrix})$ is an eigenpair of (3.2). With $\omega \neq 0$ it holds that $\mathbf{h} = \iota(\gamma I^{(i)} -$

7

$\omega^{-1}C)\mathbf{e}$. Note that A_γ, B_γ in (3.2) are Hermitian with A_γ being indefinite; (A_γ, B_γ) is regular (i.e., $\det(A_\gamma - \omega B_\gamma) \not\equiv 0$) if $\gamma \neq \sqrt{\varepsilon_i}$; For $\gamma < \sqrt{\varepsilon_i}$, the matrix pair (A_γ, B_γ) with $B_\gamma > 0$ being positive definite has all real eigenvalues [8]; For $\gamma > \sqrt{\varepsilon_i}$, B_γ is indefinite and (A_γ, B_γ) may have complex eigenvalues.

We now study the eigenstructure of the critical case when $\gamma = \gamma^* = \sqrt{\varepsilon_i}$. For this case, from (3.2) we have

$$A_{\gamma^*} = \begin{bmatrix} 0 & -\iota C \\ \iota C^H & -\gamma^*[I^{(i)}C + C^H I^{(i)}] \end{bmatrix}, \ B_{\gamma^*} = \begin{bmatrix} I_{3n} & 0 \\ 0 & \varepsilon_0 I^{(0)} \end{bmatrix}. \qquad (3.3)$$

It is easily checked that $\mathcal{N}(B_{\gamma^*}) = \mathcal{R}\left(\begin{bmatrix} 0 \\ \widehat{I}^{(i)} \end{bmatrix}\right)$, where $\widehat{I}^{(i)}$ is defined in Notations of Section 1. From Theorem 2.2, it follows that $\mathcal{N}(C) = \mathcal{R}((I_3 \otimes T)\Pi_0)$ and $\mathcal{N}(C^H) = \mathcal{R}((I_3 \otimes T)\bar{\Pi}_0)$. Thus, $\mathcal{N}(A_{\gamma^*}) = \mathcal{R}(N_{\gamma^*})$, where

$$N_{\gamma^*} = \begin{bmatrix} -\iota \gamma^* I^{(i)}(I_3 \otimes T)\Pi_0 & (I_3 \otimes T)\bar{\Pi}_0 \\ (I_3 \otimes T)\Pi_0 & 0 \end{bmatrix}. \qquad (3.4)$$

Theorem 3.1. *It holds generically that $\mathcal{N}(A_{\gamma^*}) \cap \mathcal{N}(B_{\gamma^*}) = \{0\}$.*

Proof. Let $\mathbf{x} \in \mathcal{N}(A_{\gamma^*}) \cap \mathcal{N}(B_{\gamma^*})$. Then there are $\mathbf{z}_1 \in \mathbb{C}^{2n}, \mathbf{z}_2 \in \mathbb{C}^{n_i}$ with n_i being the number of columns of $\widehat{I}^{(i)}$ such that $\mathbf{x} = N_{\gamma^*}\mathbf{z}_1 = \begin{bmatrix} 0 \\ \widehat{I}^{(i)} \end{bmatrix} \mathbf{z}_2$. It follows that

$$\tilde{N}_{\gamma^*}\mathbf{z} \equiv \left[N_{\gamma^*} \ \middle| \ \begin{matrix} 0 \\ -\widehat{I}^{(i)} \end{matrix} \right] \begin{bmatrix} \mathbf{z}_1 \\ \mathbf{z}_2 \end{bmatrix} = 0 \qquad (3.5)$$

with $\tilde{N}_{\gamma^*} \in \mathbb{C}^{6n \times (2n+n_i)}$. $\tilde{N}_{\gamma^*}$ is generically of full column rank. This implies that $\mathbf{z} = 0$, and thus $\mathbf{x} = 0$. ∎

Theorem 3.2. *Suppose that the $n_i \times n_i$ submatrix $\widehat{I}^{(i)\top}(C + C^H)\widehat{I}^{(i)}$ in A_{γ^*} has nullity $\hat{n}_i \geq 1$. Then the matrix pencil $A_{\gamma^*} - \omega B_{\gamma^*}$ in (3.2) has at least $\hat{n}_i$ 2×2 Jordan blocks at $\omega = \infty$.*

Proof. From the assumption that $\widehat{I}^{(i)\top}(C + C^H)\widehat{I}^{(i)}$ in A_{γ^*} corresponding to the $n_i \times n_i$ zero diagonal block of $\varepsilon_0 I^{(0)}$ in B_{γ^*} has a nullspace of dimension $\hat{n}_i$. Because of $\mathcal{N}(A_{\gamma^*}) \cap \mathcal{N}(B_{\gamma^*}) = \{0\}$ as in Theorem 3.1, from Theorem 4.1 of [9], $A_{\gamma^*} - \omega B_{\gamma^*}$ has at least $\hat{n}_i$ 2×2 Jordan blocks at $\omega = \infty$. ∎

Remark 3.1. *In fact, the condition of the singularity of $\widehat{I}^{(i)\top}(C + C^H)\widehat{I}^{(i)}$ in Theorem 3.2 heavily depends on shapes of materials in (1.4). This condition always holds for our numerical examples in Section 5.3.*

Theorem 3.3. *For $\gamma^+ = \gamma^* + \eta$ as $\eta \to 0^+$, it holds that $A_{\gamma^+} - \omega B_{\gamma^+}$ has at least one complex conjugate eigenvalue pairs of the forms*

$$\omega_\pm(\gamma^+) := \frac{1}{1+\eta} \pm \frac{\iota}{\sqrt{\eta}(1+\eta)}, \ \ as \ \eta \to 0^+. \qquad (3.6)$$

8

Proof. From Theorem 3.2, $A_{\gamma^*} - \omega B_{\gamma^*}$ has at least one 2×2 Jordan form at $\omega = \infty$. Therefore, $A_{\gamma^+} - \omega B_{\gamma^+}$ must have a canonical sub-block of the form $\begin{bmatrix} 0 & 1 \\ 1 & 0 \end{bmatrix} - \omega \begin{bmatrix} 1 & \eta \\ \eta & -\eta \end{bmatrix}$, as $\eta \to 0^+$. Here, for convenience, we write $\eta \equiv \mathcal{O}(\eta) > 0$ with "$\mathcal{O}$" denoting the big O. Thus, we have $\eta\omega^2 + (1 - \eta\omega)^2 = 0$ solving which we get (3.6). $\blacksquare$

Discussion 1. (i) *Let $[(\mathbf{h} - \iota\gamma I^{(i)}\mathbf{e})^\top, \mathbf{e}^\top]^\top$ be the eigenvector of $A_\gamma - \omega B_\gamma$ in (3.2) corresponding to ω. Then it holds that*

$$c(\mathbf{e}) - \omega\gamma b(\mathbf{e}) - \omega^2[\varepsilon_0 a_0(\mathbf{e}) + (\varepsilon_i - \gamma^2)a_i(\mathbf{e})] = 0, \tag{3.7}$$

where

$$c(\mathbf{e}) = \mathbf{e}^H C^H C \mathbf{e} \geq 0, \quad b(\mathbf{e}) = \mathbf{e}^H \left[I^{(i)}C + C^H I^{(i)} \right] \mathbf{e}, \tag{3.8a}$$

$$a_0(\mathbf{e}) = \mathbf{e}^H I^{(0)}\mathbf{e} \geq 0, \quad a_i(\mathbf{e}) = \mathbf{e}^H I^{(i)}\mathbf{e} = \mathbf{e}^H\mathbf{e} - a_0(\mathbf{e}) \geq 0. \tag{3.8b}$$

Then we have

$$\omega_\pm(\gamma) = \frac{\gamma b(\mathbf{e}) \pm \sqrt{\Delta(\mathbf{e})}}{-2[\varepsilon_0 a_0(\mathbf{e}) + (\varepsilon_i - \gamma^2)a_i(\mathbf{e})]} \tag{3.9}$$

with

$$\Delta(\mathbf{e}) = \gamma^2 b(\mathbf{e})^2 + 4c(\mathbf{e})[\varepsilon_0 a_0(\mathbf{e}) + (\varepsilon_i - \gamma^2)a_i(\mathbf{e})]$$
$$= \gamma^2 b(\mathbf{e})^2 + 4c(\mathbf{e})[(\varepsilon_0 + \gamma^2 - \varepsilon_i)a_0(\mathbf{e}) + (\varepsilon_i - \gamma^2)\mathbf{e}^H\mathbf{e}]. \tag{3.10}$$

From Theorem 3.3, when $\gamma^+ = \gamma^* + \eta$ (as $\eta \to 0^+$) with $\Delta(\mathbf{e}) < 0$, it must hold that $a_0(\mathbf{e}) \approx 0$ and $b(\mathbf{e}) \approx 0$. Thus, $\mathbf{e}^{(0)} \equiv I^{(0)}\mathbf{e} \approx 0$, i.e., at $\gamma = \gamma^+$, the electric field $\mathbf{E}(\mathbf{x})$ *almost vanish* *when $\mathbf{x}$ is outside the material.*

(ii) *We increase γ^+ to γ^0 so that two complex conjugate eigenvalues $\omega_\pm(\gamma)$ collide on the real axis at $\gamma = \gamma^0$ with $\Delta(\mathbf{e}) = 0$ and create (bifurcate into) two new real eigenvalues $\omega_\pm(\gamma^1)$ with $\gamma^1 > \gamma^0$ in which $\omega_+(\gamma^1) > 0$ is the smallest one among other existing positive real eigenvalues. In this case, from (3.9) and (3.8), we see that $a_0(\mathbf{e}) \approx \mathcal{O}(\eta)$ and $b(\mathbf{e}) \approx \mathcal{O}(1)$ with* *small* *$\eta > 0$. This implies that at $\gamma = \gamma^1$, the electric field $\mathbf{E}(\mathbf{x})$ is also flat when $\mathbf{x}$ is outside the material (see numerical experiments in Section 5.5).*

(iii) *Interchanging the roles of μ_d and ε_d as well as $\mathbf{h}$ and $\mathbf{e}$ in (1.7),* *similarly to (3.1) and (3.2)**, we have the matrix pencil*

$$\begin{bmatrix} -\gamma[I^{(i)}\tilde{C}^H + \tilde{C}I^{(i)}] & -\iota\tilde{C} \\ \iota\tilde{C}^H & 0 \end{bmatrix}$$
$$- \omega \begin{bmatrix} \varepsilon_0 I^{(0)} + (\varepsilon_i - \gamma^2)I^{(i)} & 0 \\ 0 & I_{3n} \end{bmatrix} \tag{3.11}$$

with the eigenpair $(\omega, \begin{bmatrix} \mathbf{h} \\ \tilde{\mathbf{e}} - \iota\gamma I^{(i)}\tilde{\mathbf{h}} \end{bmatrix})$, *where* $\tilde{C} = \varepsilon_d^{1/2} C \varepsilon_d^{-1/2}$, $\tilde{\mathbf{h}} = \varepsilon_d^{-1/2}\mathbf{h}$ *and* $\tilde{\mathbf{e}} = \varepsilon_d^{1/2}\mathbf{e}$. *As in (3.7)-(3.10), it also holds that*

$$\omega_{\pm}(\gamma) = \frac{-\gamma\tilde{b}(\tilde{\mathbf{h}}) + \sqrt{\tilde{\Delta}(\tilde{\mathbf{h}})}}{-2[\varepsilon_0\tilde{a}_0(\tilde{\mathbf{h}}) + (\varepsilon_i - \gamma^2)\tilde{a}_i(\tilde{\mathbf{h}})]} \tag{3.12}$$

with $\tilde{\Delta}(\tilde{\mathbf{h}}) = \gamma^2\tilde{b}(\tilde{\mathbf{h}})^2 + 4\tilde{c}(\tilde{\mathbf{h}})[\varepsilon_0\tilde{a}_0(\tilde{\mathbf{h}}) + (\varepsilon_i - \gamma^2)\tilde{a}_i(\tilde{\mathbf{h}})]$, *where*

$$\tilde{a}_0(\tilde{\mathbf{h}}) = \tilde{\mathbf{h}}^H I^{(0)}\tilde{\mathbf{h}} \geq 0, \tag{3.13a}$$

$$\tilde{a}_i(\tilde{\mathbf{h}}) = \tilde{\mathbf{h}}^H I^{(i)}\tilde{\mathbf{h}} \geq 0, \tag{3.13b}$$

$$\tilde{b}(\tilde{\mathbf{h}}) = \tilde{\mathbf{h}}^H [I^{(i)}\tilde{C}^H + \tilde{C}I^{(i)}]\tilde{\mathbf{h}} \in \mathbb{R}, \tag{3.13c}$$

$$\tilde{c}(\tilde{\mathbf{h}}) = \tilde{\mathbf{h}}^H \tilde{C}^H \tilde{C}\tilde{\mathbf{h}} \geq 0. \tag{3.13d}$$

As in (ii), we can also conclude that for $\omega_+(\gamma^1)$ *with* $\gamma^1 > \gamma^*$ *the smallest eigenvalue among the other existing positive real eigenvalues, the associated magnetic field* $\boldsymbol{H}(\mathbf{x})$ *is flat when* $\mathbf{x}$ *is outside the material.*

4. Null-space free method with shift-invert residual Arnoldi method

Since the $6n \times 6n$ Hermitian matrix A_γ in (3.2) has a huge null space with nullity $2n$, it would significantly affect and slow down the convergence of smallest positive eigenvalues. To remedy this drawback, we develop an efficient numerical algorithm for the computation of a few smallest positive eigenpairs of (1.7) by applying the SIRA to the $4n \times 4n$ null-space free GEP (NFGEP) derived in [8].

Theorem 4.1 ([8]). *If* $\gamma \neq \gamma^*$, *then the GEP in (1.7) can be reduced to a* $4n \times 4n$ *NFGEP*

$$\widehat{A}_r\mathbf{y}_r = \omega \left(\iota \begin{bmatrix} 0 & \Sigma_r^{-1} \\ -\Sigma_r^{-1} & 0 \end{bmatrix} \right)\mathbf{y}_r \equiv \omega\widehat{B}_r\mathbf{y}_r, \tag{4.1}$$

and

$$\begin{bmatrix} \mathbf{h}^\top & \mathbf{e}^\top \end{bmatrix}^\top = \iota \begin{bmatrix} -I_{3n} & -\zeta_d \\ \xi_d & \varepsilon_d \end{bmatrix}^{-1} \mathrm{diag}\left(P_r, Q_r\right)\mathbf{y}_r,$$

where

$$\widehat{A}_r := \widehat{A}_r(\gamma) \equiv \mathrm{diag}(P_r^H, Q_r^H) \begin{bmatrix} \zeta_d & -I_{3n} \\ I_{3n} & 0 \end{bmatrix} \begin{bmatrix} \Phi^{-1} & 0 \\ 0 & I_{3n} \end{bmatrix} \begin{bmatrix} \xi_d & I_{3n} \\ -I_{3n} & 0 \end{bmatrix} \mathrm{diag}(P_r, Q_r) \tag{4.2}$$

with $\Phi := \Phi(\gamma) \equiv \varepsilon_d - \xi_d\zeta_d$ *being Hermitian.*

Form (3.7)-(3.10) it follows that for $\gamma > \gamma^*$, each complex eigenvalue of (A_γ, B_γ) in (3.2) appears in a complex conjugate pair. In the following theorem, we further show that the eigenvalues of the null-space free matrix pair $(\widehat{A}_r, \widehat{B}_r)$ in (4.1) have the common property as the complex Hamiltonian matrix.

Theorem 4.2. *For $\gamma > \gamma^*$, if ω is a complex eigenvalue of $(\widehat{A}_r, \widehat{B}_r)$ as in (4.1), then $\bar{\omega}$ is also an eigenvalue.*

Proof. Let $\mathbf{y} = \begin{bmatrix} 0 & \Sigma_r^{-1/2} \\ \Sigma_r^{-1/2} & 0 \end{bmatrix} \mathbf{y}_r$. Then the equation (4.1) can be rewritten as

$$\mathcal{H}\mathbf{y} \equiv \begin{bmatrix} \Sigma_r^{1/2} & 0 \\ 0 & -\Sigma_r^{1/2} \end{bmatrix} \widehat{A}_r \begin{bmatrix} 0 & \Sigma_r^{1/2} \\ \Sigma_r^{1/2} & 0 \end{bmatrix} \mathbf{y} = \iota\omega\mathbf{y}. \tag{4.3}$$

With $J = \begin{bmatrix} 0 & I \\ -I & 0 \end{bmatrix}$, it is easy to check that

$$\mathcal{H}J = -J \begin{bmatrix} 0 & \Sigma_r^{1/2} \\ \Sigma_r^{1/2} & 0 \end{bmatrix} \widehat{A}_r \begin{bmatrix} \Sigma_r^{1/2} & 0 \\ 0 & -\Sigma_r^{1/2} \end{bmatrix} = -J\mathcal{H}^H.$$

So, $\mathcal{H}$ is a complex Hamiltonian matrix. It follows that if $\lambda = \iota\omega$ is an eigenvalue of $\mathcal{H}$, then $-\bar{\lambda} = \iota\bar{\omega}$ is also an eigenvalue of $\mathcal{H}$. Therefore, each complex eigenvalue appears in a complex conjugate pair. ∎

For the case $\gamma < \gamma^*$, the diagonal matrix Φ in (4.2) is positive definite, so $\widehat{A}_r$ in (4.2) is also Hermitian and positive definite. This means that all eigenvalues in (4.1) are positive real [8] and the inverse Lanczos method can be applied to solve (4.1). In each step of the inverse Lanczos method, the crucial linear system $\widehat{A}_r\mathbf{u} = \mathbf{b}$ can be efficiently solved by the conjugate gradient (CG) method without any preconditioner [8, 13]. However, for the case $\gamma > \gamma^*$, Φ in (4.2) is indefinite. So, both $\widehat{A}_r$ and $\widehat{B}_r$ are indefinite. The inverse Lanczos method with the CG-method can no longer be applied for solving (4.1).

In general, the shift-invert Arnoldi method can be used to find a few of the smallest positive eigenvalues of the NFGEP (4.1). However, in each iteration of the shift-and-invert Arnoldi method, a highly accurate solution of the linear system

$$\left(\widehat{A}_r - \sigma\widehat{B}_r\right)\mathbf{z} \equiv \left(\widehat{A}_r - \iota\sigma\begin{bmatrix} 0 & \Sigma_r^{-1} \\ -\Sigma_r^{-1} & 0 \end{bmatrix}\right)\mathbf{z} = \mathbf{c} \tag{4.4}$$

with a shift σ is required, which in practice is quite expensive. To remedy this drawback, we consider the inexact SIRA method [13, 15, 16, 20] for solving (4.1). In fact, the SIRA is designed to find a few of the eigenvalues that are close to the shift value σ. The SIRA is mathematically equivalent to the Arnoldi method in exact arithmetic [20]. The framework of the inexact SIRA is similar to the Jacobi-Davidson method. Given an orthonormal matrix $V_m = [\mathbf{v}_1, \ldots, \mathbf{v}_m]$, let $(\theta, \mathbf{y})$ be the Ritz pair of $(\widehat{A}_r, \widehat{B}_r)$ with respect to V_m. To compute the additional basis vector $\mathbf{v}_{m+1}$ in each iteration, the SIRA first approximately solves the linear system

$$\left(\widehat{A}_r - \sigma\widehat{B}_r\right)\mathbf{v} = \mathbf{r} \tag{4.5}$$

for the residual vector $\mathbf{r} = \widehat{A}_r\mathbf{y} - \theta\widehat{B}_r\mathbf{y}$. The basis vector $\mathbf{v}_{m+1}$ is then computed by orthogonalizing $\mathbf{v}$ against V_m. We summarize the process of inexact SIRA in Algorithm 1.

Algorithm 1 The Shift-Invert Residual Arnoldi method for solving $\widehat{A}_r\mathbf{y} = \omega\widehat{B}_r\mathbf{y}$.

Require: Hermitian coefficient matrices $\widehat{A}_r$ and $\widehat{B}_r$, the number of desired eigenvalues ℓ, an initial vector V_1, target σ, tolerance ϵ and number of Ritz vectors m.

Ensure: The desired eigenpairs $(\omega_j, \mathbf{y}_j)$ for $j = 1, \ldots, \ell$.

1: Set $V_\mathbf{y} = [\ ]$, $k = 1$ and $\mathbf{r}_0 = \mathbf{e}_1$.

2: **for** $j = 1, \ldots, \ell$ **do**

3:     Compute $W_k = \widehat{A}_r V_k$, $Z_k = \widehat{B}_r V_k$, $M_k = V_k^H W_k$ and $N_k = V_k^H Z_k$.

4:     **while** ($\|\mathbf{r}_{k-1}\|_2 \geq \varepsilon$) **do**

5:         Compute the eigenpairs $(\theta_i, \mathbf{s}_i)$ of $M_k\mathbf{s} = \theta N_k\mathbf{s}$ with $\|\mathbf{s}_i\|_2 = 1$. Assume $\theta_1 > 0$ is the closest to σ.

6:         Compute $\mathbf{u}_k = V_k\mathbf{s}_1$ and $\mathbf{r}_k = (\widehat{A}_r - \theta_1\widehat{B}_r)\mathbf{u}_k$.

7:         **if** ($\|\mathbf{r}_k\|_2 < \epsilon$), set $\lambda_j = \theta_1$, $\mathbf{y}_j = \mathbf{u}_k$, $k := k + 1$. Go to line 4.

8:         Solve (approximately) a $\mathbf{t}_k$ from

$$(\widehat{A}_r - \sigma\widehat{B}_r)\mathbf{t}_k = \mathbf{r}_k. \tag{4.6}$$

9:         Orthogonalize $\mathbf{t}_k$ against V_k; set $\mathbf{v}_{k+1} = \mathbf{t}_k/\|\mathbf{t}_k\|$.

10:        Compute $\mathbf{w}_{k+1} = \widehat{A}_r\mathbf{v}_{k+1}$, $M_{k+1} = \begin{bmatrix} M_k & V_k^H\mathbf{w}_{k+1} \\ \mathbf{v}_{k+1}^H W_k & \mathbf{v}_{k+1}^H\mathbf{w}_{k+1} \end{bmatrix}$.

11:        Compute $\mathbf{z}_{k+1} = \widehat{B}_r\mathbf{v}_{k+1}$, $N_{k+1} = \begin{bmatrix} N_k & V_k^H\mathbf{z}_{k+1} \\ \mathbf{v}_{k+1}^H Z_k & \mathbf{v}_{k+1}^H\mathbf{z}_{k+1} \end{bmatrix}$.

12:        Expand $V_{k+1} = [V_k, \mathbf{v}_{k+1}]$, $W_{k+1} = [W_k, \mathbf{w}_{k+1}]$ and $Z_{k+1} = [Z_k, \mathbf{z}_{k+1}]$. Set $k := k + 1$.

13:     **end while**

14:     Set $V_\mathbf{y} = [V_\mathbf{y}, \mathbf{y}_j]$, $V_{j+m-1} = [V_\mathbf{y}, V_{k-1}[\mathbf{s}_2, \cdots, \mathbf{s}_m]]$, $k = j + m - 1$ and $\mathbf{r}_{k-1} = \mathbf{e}_1$.

15: **end for**

It has been shown in [16] that when the relative error of the approximate solution of (4.5) is modestly small at each iteration, the inexact SIRA mimics the exact SIRA well. The numerical results in [13] also demonstrate that the inexact SIRA is effective even the relative error is only 5×10^{-4}. Since the coefficient matrix $\widehat{A}_r - \sigma\widehat{B}_r$ in (4.5) is Hermitian, we use MINRES without any preconditioner to solve (4.5). Based on the results in [13, 16], the stopping criterion is taken as 10^{-3}. A heuristic strategy in Algorithm 2 is utilized to determine the maximum iteration number m_k of MINRES.

Remark 4.1. *As $\widehat{A}_r$ in (4.2) with (P_r, Q_r) in (2.6) as well as ζ_d, ξ_d, Φ, and Λ_j $(j = 1, 2, 3)$ being diagonal matrices, the main computational cost for solving*

Algorithm 2 The heuristic strategy for determining the maximal iteration m_k of MINRES in solving (4.6) approximately.

Require: $m_0 = 1000$, m_{k-1}, residual vectors $\mathbf{r}_{k-1}$ and $\mathbf{r}_k$.
Ensure: The maximal iteration m_k.
1: **if** $\|\mathbf{r}_k\|_2 \geq 0.1$ and $k > 14$ **then**
2:     Set $m_k = 2000$;
3: **else if** $\|\mathbf{r}_k\|_2 < 0.1$ and $\|\mathbf{r}_{k-1}\|_2/\|\mathbf{r}_k\|_2 < 4$ **then**
4:     Set $m_k = \min(2000, m_{k-1} + 100)$;
5: **else**
6:     Set $m_k = m_{k-1}$;
7: **end if**

(4.5) *by using MINRES is the matrix-vector multiplications $T^H \mathbf{p}$ and $T\mathbf{q}$, where T is defined in Theorem 2.1. As shown in [11], these matrix-vector multiplications can be computed efficiently by the FFT-based schemes without explicitly forming matrix T. Therefore the matrix-vector multiplication with matrix $\widehat{A}_r - \sigma \widehat{B}_r$ in each iteration can be computed effectively.*

5. Numerical experiments

To study numerical behaviors of the 3D Maxwell's equations for reciprocal chiral media (2.8b) with $\gamma > \sqrt{\varepsilon_i}$ in (2.8a), we consider the FCC lattice [11] which consists of dielectric spheres with connecting spheroids as shown in Figure 1. The radius r of the spheres and the minor axis length s of the spheroids are $r = 0.08a$ and $s = 0.06a$, respectively, where a is the lattice constant. The perimeter of the irreducible Brillouin zone for the lattice is formed by the corners $X = \frac{2\pi}{a}\Omega[0,1,0]^\top$, $U = \frac{2\pi}{a}\Omega\left[\frac{1}{4},1,\frac{1}{4}\right]^\top$, $L = \frac{2\pi}{a}\Omega\left[\frac{1}{2},\frac{1}{2},\frac{1}{2}\right]^\top$, $G = [0,0,0]^\top$, $W = \frac{2\pi}{a}\Omega\left[\frac{1}{2},1,0\right]^\top$, and $K = \frac{2\pi}{a}\Omega\left[\frac{3}{4},\frac{3}{4},0\right]^\top$, where

$$\Omega = \frac{1}{\sqrt{2}}\begin{bmatrix} 1 & 1 & 0 \\ -\frac{1}{\sqrt{3}} & \frac{1}{\sqrt{3}} & \frac{2}{\sqrt{3}} \\ \frac{2}{\sqrt{6}} & -\frac{2}{\sqrt{6}} & \frac{2}{\sqrt{6}} \end{bmatrix}.$$

Here, we take the permittivity ε_i to be 13 and then $\gamma^* = \sqrt{13} \approx 3.606$.

All computations in this section are carried out in MATLAB 2017a, and the MATLAB functions `fft` and `ifft` are used to compute the matrix-vector multiplications $T^H \mathbf{p}$ and $T\mathbf{q}$, respectively, as mentioned in Remark 4.1. The mesh numbers n_1, n_2 and n_3 are taken as $n_1 = n_2 = n_3 = 96$ and the matrix dimension of $\widehat{A}_r$ in (4.2) is 3,538,944. Furthermore, the stopping tolerance for the inexact SIRA is set to be 10^{-12}.

5.1. Iteration numbers for solving linear systems (4.5)

First, we discuss iteration numbers of MINRES without any preconditioner for solving linear systems (4.5). The stopping tolerance of MINRES is set to be 10^{-3}. The wave vector $\mathbf{k}$ is chosen to be $\frac{13}{14}X + \frac{1}{14}U$.
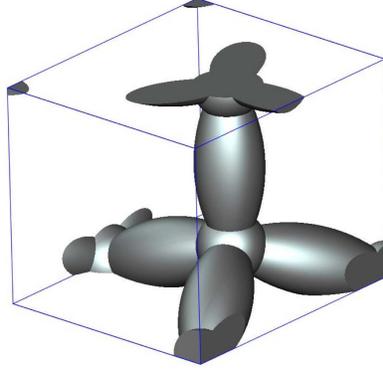
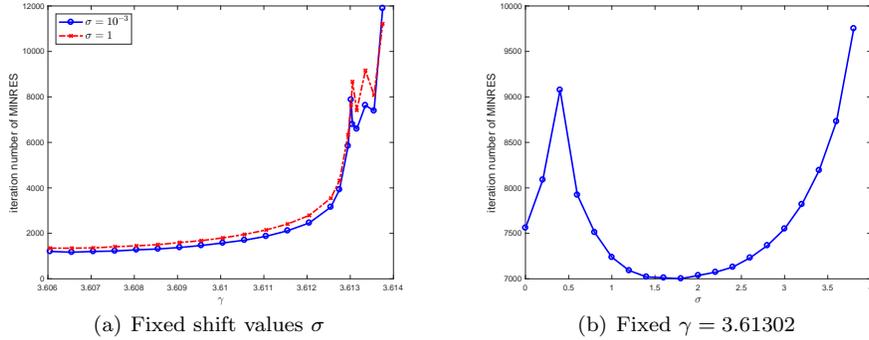Figure 1: A schema of 3D complex media with the FCC lattice within a single primitive cell.

(a) Fixed shift values σ

(b) Fixed $\gamma = 3.61302$

Figure 2: Iteration numbers of MINRES with the stopping tolerance 10^{-3} for solving (4.5).

The shift values σ in (4.5) are taken as 10^{-3} and 1. The associated iteration numbers vs. various γ are shown in Figure 2(a). We see that the numbers of iterations for $\sigma = 10^{-3}$ and $\sigma = 1$ are similar and smoothly increasing as γ raises to 3.612. However, after $\gamma = 3.612$, the numbers of iterations become significantly large (≥ 6000) when $\gamma \geq 3.613$.

Now, we demonstrate iteration numbers vs. shifts σ with a fixed γ. Taking $\gamma = 3.61302$ in Figure 2(b), we show the iteration numbers vs. various shift values σ. We observe that no matter which shift value is chosen the iteration numbers range from 7,000 to 10,000. Most of them are significantly greater than 7,000. This means that solving the linear system (4.5) is a difficult task. Therefore, Arnoldi method, which needs more accurate solution of (4.5), is not suitable for solving the NFGEP (4.1). This is the reason why we prefer the inexact SIRA method over Arnoldi method for solving (4.1).

(a) $\gamma = 3.607$ (b) $\gamma = 3.61302$
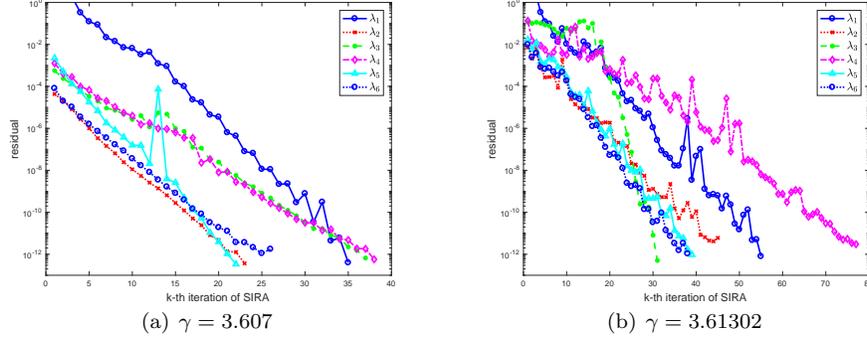
Figure 3: Convergence behaviors of SIRA with the stopping tolerance 10^{-12} for computing six smallest positive eigenvalues of NFGEP (4.1).

5.2. Convergence of SIRA for solving NFGEP (4.1)

As shown in [13, 16], the relative error of the approximate solution of (4.5) can be modestly small at each iteration of the inexact SIRA. We take the stopping tolerance for solving (4.5) to be 10^{-3}. Based on the iteration numbers shown in Figure 2, it needs more than 6,000 iterations to achieve this tolerance when $\gamma \geq 3.613$. The computational cost becomes very high. In order to reduce the cost, but still keep the approximation in solving (4.5), we give a heuristic strategy for determining the maximal iteration of MINRES in Algorithm 2.

In Figure 3, we show the convergence behavior for computing six smallest positive eigenvalues $\lambda_1, \ldots, \lambda_6$ by using the inexact SIRA. For $\gamma = 3.607$, because most of the relative errors of approximate solutions for (4.5) are less than the stopping tolerance, the iteration numbers of the inexact SIRA for computing $\lambda_1, \ldots, \lambda_6$ range from 22 to 38 as shown in Figure 3(a). For $\gamma = 3.61302$, even all relative errors are larger than the stopping tolerance (i.e., all iterations are reached the maximal iteration numbers defined in Algorithm 2), we can see that the iteration numbers of the inexact SIRA still range from 31 to 77 as shown in Figure 3(b). All results demonstrate that the target eigenpairs can be computed by Algorithm 1 combined with Algorithm 2 in a reasonable iteration number.

5.3. Falling down new smallest positive eigenvalues

In Theorem 3.2, we prove that the matrix pencil $A_\gamma - \omega B_\gamma$ in (3.2) with $\gamma = \gamma^* = \sqrt{\varepsilon_i}$ has at least $\hat{n}_i$ 2×2 Jordan blocks at $\omega = \infty$. Theorem 3.3 shows that such infinite eigenvalues with 2×2 Jordan block will split into two complex conjugate eigenvalues $\lambda_1(\gamma)$ and $\bar{\lambda}_1(\gamma)$ as $\gamma \to \sqrt{\varepsilon_i} + 0^+$.

Note that, in our test examples for the FCC lattice, we check the submatrix $\widehat{I}^{(i)\top}(C + C^H)\widehat{I}^{(i)}$ in Theorem 3.2 having at least 30 zero eigenvalues, which shows that the existence of the positive nullity $\hat{n}_i$ in Theorem 3.2 indeed happens.

(a) Conjugate eigenvalue pair $(\lambda(\gamma), \bar{\lambda}(\gamma))$

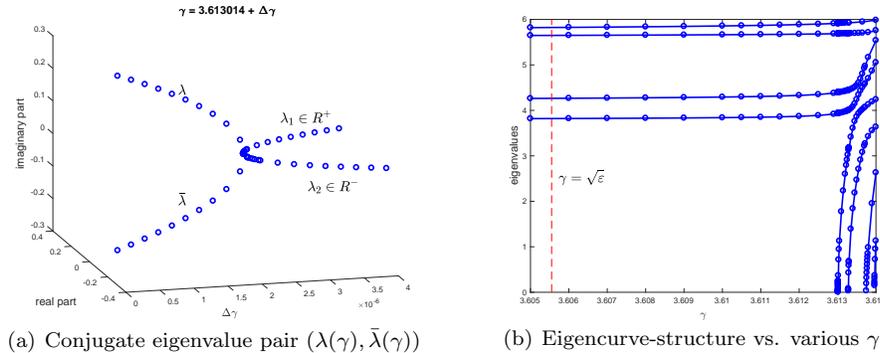(b) Eigencurve-structure vs. various γ

Figure 4: Conjugate eigenvalue pair and eigencurve-structure with $\mathbf{k} = \frac{13}{14}X + \frac{1}{14}U$.

Now, we verify the existence of the conjugate eigenvalue pair $(\lambda(\gamma), \bar{\lambda}(\gamma))$ by numerical experiments. First, we compute the first two eigenvalues with the smallest module as shown in Figure 4(a). The results show that there is a complex conjugate eigenvalue pair $(\lambda(\gamma), \bar{\lambda}(\gamma))$ for $\gamma \in [3.6130144, 3.6130162]$. The positive imaginary part of $\lambda(\gamma)$ is dramatically decreasing, and then $\lambda(\gamma)$ and $\bar{\lambda}(\gamma)$ bifurcate, respectively, into positive and negative eigenvalues $\lambda_1 > 0$ (resonance mode), $\lambda_2 < 0$ near $\gamma = 3.613016273$.

The result in Figure 4(a) shows the existence of a pair of complex conjugate eigenvalues which collide together at some $\gamma = \gamma_0 > \gamma^*$, after γ_0, and bifurcate into a positive and a negative eigenvalue. Actually, there are many complex conjugate eigenvalue pairs which bifurcate at various γ with $\gamma > \gamma_0$. In Figure 4(b), we show the eigencurve structure vs. various γ and see that four resonance modes bifurcate from four conjugate eigenvalue pairs which emerge from lower frequencies and push the original eigenmodes to higher frequencies when γ ranges from 3.613 to 3.614. The values of resonance modes increase rapidly as γ increases.

Note that, comparing the results of Figure 2(a) and Figure 4(b), we find that the iteration number of MINRES dramatically increase when the resonance modes appear.

5.4. Anticrossing eigencurves

In this subsection, we discuss the influence of the resonance modes for band structures. Three fully band structures with different γ are shown in Figure 5. For the critical case that $\gamma = 3.607 \approx \gamma^* = \sqrt{13}$, the associated band structure in Figure 5(a) inherits the structure for the case that $\gamma < \gamma^*$. Comparing band structures in Figures 5(a) and 5(b), we see that a new eigencurve emerges at $\gamma = 3.61302$ which comes from the bifurcation of the conjugate eigenvalue pair as mentioned in Section 5.3. Besides this new eigencurve, the others are similar to those in Figure 5(a). However, when $\gamma = 3.6138$, four resonance modes as
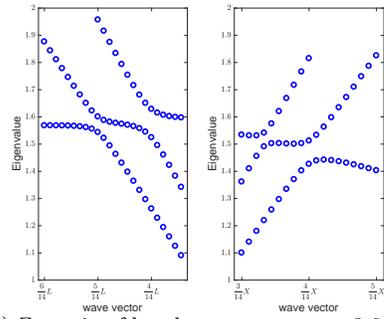
16
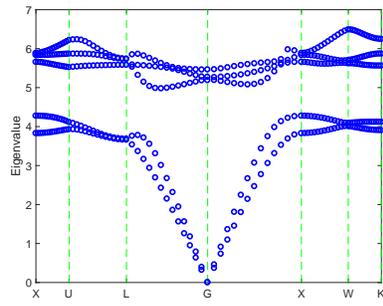
(a) $\gamma = 3.607$
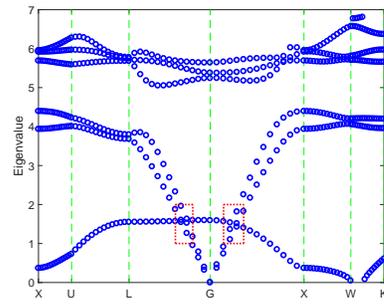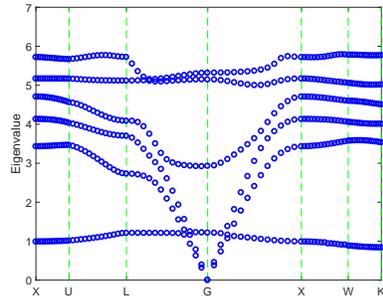
(b) $\gamma = 3.61302$

(c) $\gamma = 3.6138$

(d) Zoom-in of band structure at $\gamma = 3.61302$

Figure 5: Band structures.

shown in Figure 4(b) appear. The original eigenmodes are pushed up by these new resonance modes so that the band structure in Figure 5(c) is totally different from that in Figure 5(a). Moreover, the resonance modes in Figure 5(c) tend to be dispersionless, that is, insensitive to the change of wave vectors, and are represented by flat bands.

In Figures 5(b) and 5(c), the eigencurves of the first three smallest positive eigenvalues are close to each other near points $\frac{4}{14}L$ and $\frac{3}{14}X$, respectively. Now, we refine the partitions of the red regions in Figure 5(b) and zoom in the first three smallest positive eigenvalues in Figure 5(d). These results show that the eigencurves exhibit anticrossing phenomena which occur in the segments $\overline{LG}$ and $\overline{GX}$ of Figures 5(b) and 5(c), respectively.
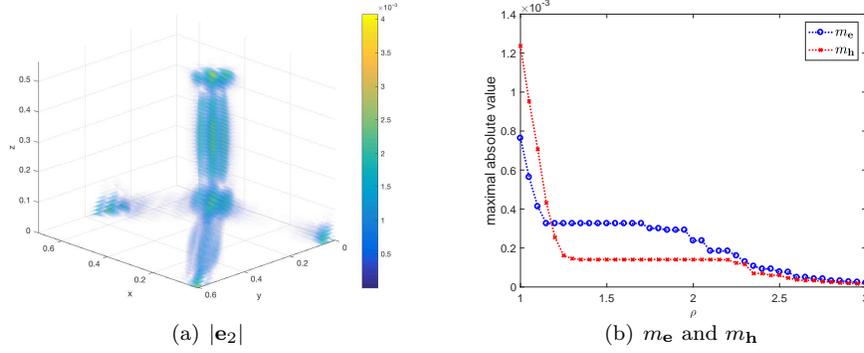

(a) $|\mathbf{e}_2|$ (b) $m_{\mathbf{e}}$ and $m_{\mathbf{h}}$

Figure 6: The absolute values of $\mathbf{e}_2$, $m_{\mathbf{e}}$, $m_{\mathbf{h}}$ for the resonance mode at $\mathbf{k} = \frac{6}{14}L$.

5.5. Condensations of eigenvectors

In this subsection, we display the entire vector $\mathbf{e}_2$ by using volumetric slice plot to validate the results in Discussion 1 of Section 3. The absolute values of $\mathbf{e}_2$ corresponding to the first smallest positive eigenvalue (resonance mode) with $\mathbf{k} = \frac{6}{14}L$ are plotted in Figures 6(a). We see that these absolute values are localized in the structure and its neighborhood that meets the shape of the 3D complex media with FCC lattice as in Figure 1. In order to measure the neighborhood, we define new radius of the sphere and the connecting spheroid to be ρr and ρs, respectively, for $\rho \geq 1$ and denote the region of these new spheres and cylinders as $D(\rho)$. Note that $D(\rho)$ for $\rho > 1$ represents the original material and its neighborhood. Let $m_{\mathbf{e}}$ and $m_{\mathbf{h}}$ denote the maximal absolute values of $\mathbf{e}$ and $\mathbf{h}$, respectively, outside $D(\rho)$. The relationship between $(m_{\mathbf{e}}, m_{\mathbf{h}})$ and ρ is plotted in Figure 6(b) which shows that all absolute values outside $D(\rho)$ are less than 4×10^{-4} for $\rho \geq 1.2$. This means that the electric field is localized in the domain $D(1.2)$ which is only $8.9\%(= \frac{\text{number of indices in } D(1.2)}{3n})$ of the whole computational domain. This phenomenon indicates that the emerging resonance
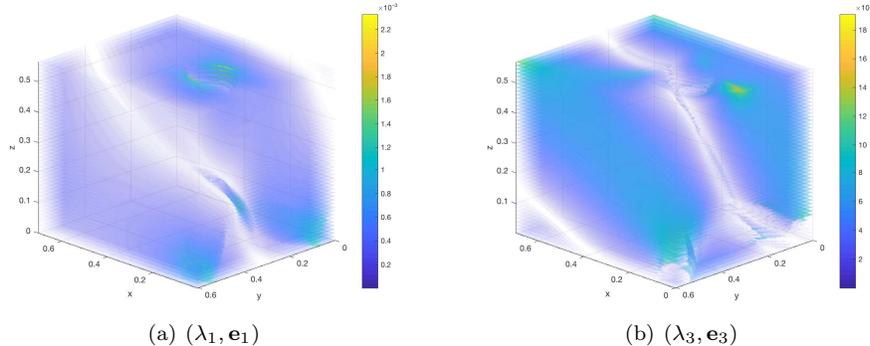
18

(a) $(\lambda_1, \mathbf{e}_1)$　　　　　　　　(b) $(\lambda_3, \mathbf{e}_3)$

Figure 7: The absolute values of the first and third eigenmodes for $\mathbf{e}_1$ and $\mathbf{e}_3$, respectively, with $\mathbf{k} = \frac{13}{14}X + \frac{1}{14}U$ and $\gamma = 1$.

mode is basically formed as a combination of the waveguide mode with highly localized in the structure and the surface plasmon mode with slightly smeared to the background material.

As shown in Figure 7, not all the electric fields for any positive γ (here $\gamma = 1$) are localized in the structure. In the following, we study the relationship between the condensation and the parameter γ. According to the mesh indices belonging to the material or not, we separate $\mathbf{e}$ and $\mathbf{h}$ as $(\mathbf{e}_i, \mathbf{e}_o)$ and $(\mathbf{h}_i, \mathbf{h}_o)$, where the index i/o denotes inside/outside the material. Since $\mathbf{e}^*\mathbf{e} + \mathbf{h}^*\mathbf{h} = 1$, we use the ratios $\frac{\mathbf{e}_o^*\mathbf{e}_o}{\mathbf{e}_i^*\mathbf{e}_i}$ and $\frac{\mathbf{h}_o^*\mathbf{h}_o}{\mathbf{h}_i^*\mathbf{h}_i}$ to determine the condensations of the electric and magnetic fields. The results in Figure 8 show that these ratios decrease as γ increases. Moreover, when the conjugate eigenvalue pair bifurcates to create resonance modes (i.e., at $\gamma \geq 3.61302$), the eigenvectors corresponding to the resonance modes are highly concentrated inside the material, with only a slight amount of fields leaking into the background (dielectric) material. This also verifies the inference in Discussion 1 of Section 3.

6. Conclusions

In this paper, we focus on the GEPs arising in the source-free Maxwell equation with magnetoelectric coupling effects in the 3D chiral media. It is a challenging problem to solve the GEP efficiently. The coefficient matrix in the discrete single-curl operator is indefinite and degenerate. A null-space free method is developed in [8] to deflate the null space from the GEP into a null-space free GEP (NFGEP). The eigenstructure behavior of the GEP is determined by the chirality parameter γ. The matrix pair in NFGEP with a small chirality γ (weakly-coupled case) is positive definite for which efficient numerical algorithms and band structures have been well-studied by Chern et al [8]; while the strongly-coupled case is still open. The difficulty is that the matrix pair in
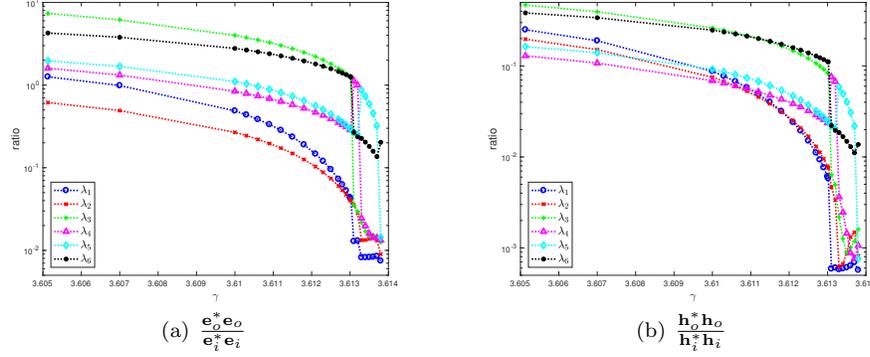
Figure 8: The ratios $\frac{\mathbf{e}_o^*\mathbf{e}_o}{\mathbf{e}_i^*\mathbf{e}_i}$ and $\frac{\mathbf{h}_o^*\mathbf{h}_o}{\mathbf{h}_i^*\mathbf{h}_i}$ for the first six smallest positive eigenvalues vs. various γ with $\mathbf{k} = \frac{13}{14}X + \frac{1}{14}U$.

NFGEP is no longer a positive definite matrix pair which may introduce a very different and complicated eigenstructure. In this article, we combine the inexact shift-invert residual Arnoldi method with MINRES linear solver for solving the NFGEP. Numerical results show that the target eigenpairs can be computed by our proposed method in a reasonable iteration number even the matrix dimension of the GEP is as large as 5,308,416. Therefore, we can use numerical results to analyze the eigenstructure behavior. For a critical value $\gamma = \gamma^*$, we show that the GEP has 2×2 Jordan blocks at infinity eigenvalues. Numerical results demonstrate that the 2×2 Jordan blocks will split into complex conjugate eigenpairs which rapidly collide on the real axis and bifurcate into a new negative eigenvalue and a new positive eigenvalue (resonance mode) which is smaller than the other existing positive eigenvalues. The resonance modes induce the anticrossing phenomena in the eigencurves. Moreover, the electric and magnetic fields of the resonance modes are concentrated inside the material structure, with only a slight amount of fields leaking into the background (dielectric) material.

Acknowledgments

Reference

[1] H. Ammari and G. Bao. Maxwells equations in periodic chiral structures. *Math. Nachr.*, 251:3–18, 2003.

[2] H. Ammari, K. Hamdache, and J.-C. Nédélec. Chirality in the Maxwell equations by the dipole approximation. *SIAM J. Appl. Math.*, 59:2045–2059, 1999.

[3] H. Ammari and J. C. Nédélec. Time harmonic electromagnetic fields in chiral media. In *Modern Mathematical Methods in Diffraction Theory and its Applications, E. Meister, Ed., Methoden Verfahren Math. Phys.*, volume 42, pages 174–202. 1997.

[4] H. Ammari and J.-C. Nédélec. Small chirality behaviour of solutions to electromagnetic scattering problems in chiral media. *Math. Meth. Appl. Sci.*, 21:327–359, 1998.

[5] H. Ammari and J. C. Nédélec. Time-harmonic electromagnetic fields in thin chiral curved layers. *SIAM J. Math. Anal.*, 29:395–423, 1998.

[6] X. Cheng, H. Chen, L. Ran, B.-I. Wu, T. M Grzegorczyk, and J. A. Kong. Negative refraction and cross polarization effects in metamaterial realized with bianisotropic s-ring resonator. *Phys. Rev. B*, 76(2):024402, 2007.

[7] R.-L. Chern. Wave propagation in chiral media: composite Fresnel equations. *J. Opt.*, 15:075702, 2013.

[8] R.-L. Chern, H.-E. Hsieh, T.-M. Huang, W.-W. Lin, and W. Wang. Singular value decompositions for single-curl operators in three-dimensional Maxwell's equations for complex media. *SIAM J. Matrix Anal. Appl.*, 36:203–224, 2015.

[9] D. Dzeng and W.W. Lin. Homotopy continuous method for the numerical solution of generalized symmetric eigenvalue problems. *J. Austral. Math. Soc. Ser. B*, 32:437–456, 1991.

[10] W. R. Ferng, W.-W. Lin, and C.-S. Wang. The shift-inverted *J*-Lanczos algorithm for the numerical solutions of large sparse algebraic Riccati equations. *Computers Math. Appl.*, 33:23–40, 1997.

[11] T.-M. Huang, H.-E. Hsieh, W.-W. Lin, and W. Wang. Eigendecomposition of the discrete double-curl operator with application to fast eigensolver for three dimensional photonic crystals. *SIAM J. Matrix Anal. Appl.*, 34:369–391, 2013.

[12] T.-M. Huang, H.-E. Hsieh, W.-W. Lin, and W. Wang. Matrix representation of the double-curl operator for simulating three dimensional photonic crystals. *Math. Comput. Model.*, 58:379–392, 2013.

[13] T.-M. Huang, H.-E. Hsieh, W.-W. Lin, and W. Wang. Eigenvalue solvers for three dimensional photonic crystals with face-centered cubic lattice. *J. Comput. Appl. Math.*, 272:350–361, 2014.

[14] T.-M. Huang, T. Li, W.-D. Li, J.-W. Lin, W.-W. Lin, and H. Tian. Solving three dimensional Maxwell eigenvalue problem with fourteen Bravais lattices. Technical report, arXiv:1806.10782, 2018.

[15] T.-M Huang, W.-W. Lin, and W. Wang. A hybrid Jacobi-Davidson method for interior cluster eigenvalues with large null-space in three dimensional lossless Drude dispersive metallic photonic crystals. *Comput. Phys. Commun.*, 207:221–231, 2016.

[16] Z. Jia and C. Li. On inner iterations in the shift-invert residual Arnoldi method and the Jacobi-Davidson method. *SCIENCE CHINA Math.*, 57:1733–1752, 2014.

[17] J. D. Joannopoulos, S. G. Johnson, J. N. Winn, and R. D. Meade. *Photonic Crystals: Molding the Flow of Light*. Princeton University Press, Princeton, NJ, 2008.

[18] C. Kittel. *Introduction to solid state physics*. Wiley, New York, NY, 2005.

[19] Jin Au Kong. Theorems of bianisotropic media. *Proc. IEEE*, 60(9):1036–1046, 1972.

[20] C. Lee. *Residual Arnoldi method: theory, package and experiments*. PhD thesis, TR-4515, Department of Computer Science, University of Maryland at College Park, 2007.

[21] J. Lekner. Optical properties of isotropic chiral media. *Pure Appl Opti: J. Euro. Opti. Soc. A*, 5(4):417–443, 1996.

[22] T. G Mackay and A. Lakhtakia. Negative refraction, negative phase velocity, and counterposition in bianisotropic materials and metamaterials. *Phys. Rev. B*, 79(23):235121, 2009.

[23] A. Serdyukov, I. Semchenko, S. Tretyakov, and A. Sihvola. *Electromagnetics of Bi-anisotropic Materials: Theory and Applications*. Gordon and Breach Science, 2001.

[24] S. A Tretyakov, C. R. Simovski, and M. Hudlička. Bianisotropic route to the realization and matching of backward-wave metamaterial slabs. *Phys. Rev. B*, 75(15):153104, 2007.

[25] W. S. Weiglhofer and A. Lakhtakia. *Introduction to Complex Mediums for Optics and Electromagnetics*. SPIE, Washington, DC, 2003.

[26] K. Yee. Numerical solution of initial boundary value problems involving Maxwell's equations in isotropic media. *IEEE Trans. Antennas and Propagation*, 14:302–307, 1966.